Available online at www.sciencedirect.com
ScienceDirect
Journal of Sound and Vibration 299 (2007) 123–142
JOURNAL OF SOUND AND VIBRATION
www.elsevier.com/locate/jsvi

Stability of a deploying/extruding beam in dense fluid

F. Gosselin, M.P. Païdoussis*, A.K. Misra

Department of Mechanical Engineering, McGill University, 817 Sherbrooke Street West, Montréal, Québec, Canada H3A 2K6

Received 19 May 2005; received in revised form 8 June 2006; accepted 30 June 2006
Available online 12 September 2006

Abstract

The equations of motion of a flexible slender cantilevered beam with uniform circular cross-section, extending axially in a horizontal plane at a known rate while immersed in an incompressible fluid are derived. An ''axial added mass coefficient'' is implemented in these equations in order to better approximate the mass of fluid which stays attached to the oscillating beam while moving in the axial direction. Realistic initial conditions are given to the system and numerical solutions are obtained. The dynamical behaviour of the system is observed for cases of constant extension rate and for a trapezoidal deployment rate profile.

In the case of low constant extension rates, the system displays a phase of oscillation with increasing amplitude and decreasing frequency until the motion is strongly damped and later becomes statically unstable. For faster deployment rates, the beam has a short flutter phase at the beginning of the deployment, followed by a brief phase of damped oscillation until it exhibits static divergence. For fast enough deployment rates, the system is unstable from the beginning and never stabilizes. The effect the axial added mass coefficient has on the system is studied and it is found that it plays two roles in the stability of the system. The trapezoidal deployment rate profile is studied because it is deemed more representative of real-life applications. For long deployment times, the system behaves in a very similar manner to one with low constant extension rate, except that it does not become statically unstable. For shorter deployment times, the maximum amplitude of the tip displacement is usually attained after the beam has stopped extruding.

1. Introduction

Motivated by the quest for a fundamental understanding of fluid–structure interactions as well as by applications in several areas of engineering, the dynamical behaviour of axially moving flexible beams has attracted the attention of several investigators. Some examples of engineering applications include, but are not limited to, extrusion processes, deployment of appendages in space (Païdoussis [1]), robotic manipulators, telescopic members of loading vehicles, and machine tools (Al-Bedoor and Khulief [2]). In all those applications, a dynamical model is essential to design and control lightweight, high precision processes or mechanisms.

An extensive review of the early literature in the domain of axially moving materials is provided by Mote [3]. It includes the work that was done in the areas of band-saws, belts, chain drives, pipes conveying fluids, and

*Corresponding author. Tel.: +1 514 398 6280; fax: +1 514 398 7365.
E-mail address: mary.fiorilli@mcgill.ca (M.P. Païdoussis).

0022-460X/$ - see front matter © 2006 Elsevier Ltd. All rights reserved.
doi:10.1016/j.jsv.2006.06.050

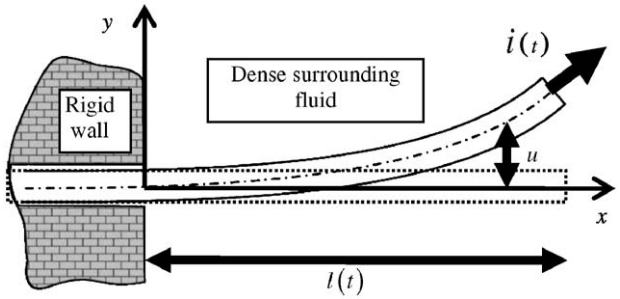

Fig. 1. The extending beam system under consideration.

other similar systems which all have in common the same (or similar) linear equation of motion and boundary conditions. More recently, Wickert and Mote [4] presented a review of more recent research in this area; more recently still, Païdoussis [1] presented a condensed review of all the work on the problem of an extruding beam.

The linearized transverse vibrations of a moving thin rod between two supports were investigated by Barakat [5]. Kalaycioglu and Misra [6] presented approximate analytical solutions to be used as benchmarks to check numerical solutions for beam-type appendage deployment and tethered system deployment. The dynamics of deployable antennas was also studied by Tabarrok and Behdinan [7]. Another analytical solution was derived by Al-Bedoor and Khulief [2]. In a study by Stylianou and Tabarrok [8,9], numerical solutions to several variations of the axially moving beam were obtained by finite element analysis.

In the previously mentioned studies, the problem was formulated such that there was no fluid surrounding the deploying beam or, if there was, it was ignored. The work done by Taleb and Misra [10] considers the dynamics of a beam of uniform circular cross-section being deployed in a dense incompressible fluid (see Fig. 1).

The present study tackles the same problem as Taleb and Misra [10]: the examination of the dynamics of a flexible slender cantilevered beam with uniform circular cross-section, extending axially in the horizontal direction at a known rate, while immersed in a dense incompressible fluid. By "extending", we understand "deploying" and "extruding", equally. Several reasons motivate a deeper analysis of the problem; mainly that it was perceived that the fluid-dynamic forces were not correctly accounted for in the analysis performed by Taleb and Misra [10]. Here, an "axial added mass coefficient" is introduced to better approximate the force of the fluid acting on the beam. This new study also allows the examination of different extension rates and a better understanding of the mechanism for static instability.

2. Development of the equation of motion

2.1. General assumptions and description of the system

Consider a cylindrical cantilevered beam extending axially in a nominally horizontal direction in the fixed reference frame as depicted in Fig. 1. Let this beam be of diameter D, with area moment of inertia I and mass per unit length m, while a complex modulus of elasticity of the material is utilized, $E_0(I+\gamma\partial/\partial t)$, where γ is a small parameter characterizing the structural damping in the beam. Consider this beam to be immersed in an incompressible fluid of density ρ, with boundaries sufficiently distant to have negligible effect on the fluid forces on the beam. Small lateral motions are considered, and it is assumed that no separation occurs in the cross-flow around the beam, and that the forces of the fluid acting on a beam element are the same as those acting on a corresponding element of a long undeformed beam of the same cross-sectional area and inclination.

In this analysis, $u(x,t)$ is the transverse displacement of an element of the beam, and the velocity of the same element can be found using the total derivative with respect to time:

$$v(x,t)=\frac{\mathrm{D}u(x,t)}{\mathrm{D}t}=\frac{\partial u}{\partial t}+\frac{\partial u}{\partial x}\frac{\partial x}{\partial t}, \tag{1}$$

where the partial derivative of x with time is equal to the extrusion rate, $\dot{l}$. Therefore, Eq. (1) becomes

$$v(x,t) = \frac{\partial u}{\partial t} + \dot{l}\,\frac{\partial u}{\partial x}. \tag{2}$$

2.2. Added mass

As the beam accelerates laterally, it creates a certain pressure field proportional to the acceleration, and hence a pressure distribution around the beam. It is convenient to express the net effect of the pressure distribution as a mass times acceleration. This mass is the added, or virtual, fluid mass and may be thought of as being effectively attached to the beam as it oscillates laterally. The virtual mass around a cylinder in a cross-flow with boundaries at infinity is generally accepted to be $m_h = \rho L\left(\frac{1}{4}\pi D^2\right)$, according to the simplest inviscid interpretation of the concept. In this study, M is the virtual mass of fluid per unit length and is defined as

$$M = \rho\left(\frac{1}{4}\pi D^2\right). \tag{3}$$

Therefore, the momentum per unit length of the virtual mass for transverse motions, i.e. motions perpendicular to the axis of the beam at equilibrium is equal to $M(\partial u/\partial t)$.

In the axial direction of the beam, the layer of fluid which stays attached to the beam is in fact considerably smaller than that of this lateral-direction virtual mass. This mass moving with the beam in the axial direction cannot be calculated by classical boundary layer theory because of the complexity generated by the oscillation. However, neglecting this mass completely is also not totally correct. As noted by Païdoussis [1, p. 856] this mass should have a value between zero and M (the lateral-direction virtual mass). In this study, this mass is taken to be equal to βM, where β is an "axial added mass coefficient" which in the calculations will be varied between zero and one (refer to Section 4.1.2). The momentum per unit length of the fluid moving in the axial direction of the beam is $\beta M\dot{l}$.

Another way of visualizing this concept is to consider the added mass to be moving with the same velocity as the cylinder in the normal direction, but only at a fraction of the velocity of the cylinder in the longitudinal direction, namely at a velocity of $\beta\dot{l}$. From this, the total time derivative for the added mass can be found:

$$\left.\frac{\mathrm{D}}{\mathrm{D}t}\right|_{\substack{\text{Added}\\ \text{mass}}} = \frac{\partial}{\partial t} + \frac{\partial x}{\partial t}\,\frac{\partial}{\partial x},$$

where the rate of change of x with respect to time is the reduced velocity $\beta\dot{l}$; hence,

$$\left.\frac{\mathrm{D}}{\mathrm{D}t}\right|_{\substack{\text{Added}\\ \text{mass}}} = \frac{\partial}{\partial t} + \beta\dot{l}\,\frac{\partial}{\partial x}. \tag{4}$$

In this paper, for clarity and economy, we use the shorthand notation of "virtual mass" for that given by Eq. (3), while the "added mass" is that attached to the beam as it is axially extended and is here taken to be equal to βM.

Differentiating the displacement according to Eq. (4), the total momentum of the fluid per unit length is found to be $M(\partial/\partial t + \beta\dot{l}\partial/\partial x)u$. Differentiating again with respect to time, the rate of change of this momentum per unit length is therefore $M(\partial/\partial t + \beta\dot{l}\partial/\partial x)^2 u$, which produces an equal and opposite lateral force on the beam.

2.3. Summation of forces

Consider a small beam element of length δx as shown in Fig. 2. Let T be the axial tension, Q the shear force, and F_L and F_N, respectively, the longitudinal and the normal viscous forces per unit length. The equations of motion are found by summing forces in the x and y directions, yielding

$$-F_L - (m + \beta M)\ddot{l} + \frac{\partial T}{\partial x} = 0, \tag{5}$$

$$\frac{\partial Q}{\partial x} - F_N - F_L\frac{\partial u}{\partial x} - m\left(\frac{\partial}{\partial t} + \dot{l}\,\frac{\partial}{\partial x}\right)^2 u - M\left(\frac{\partial}{\partial t} + \beta\dot{l}\,\frac{\partial}{\partial x}\right)^2 u + \frac{\partial}{\partial x}\left(T\frac{\partial u}{\partial x}\right) = 0. \tag{6}$$

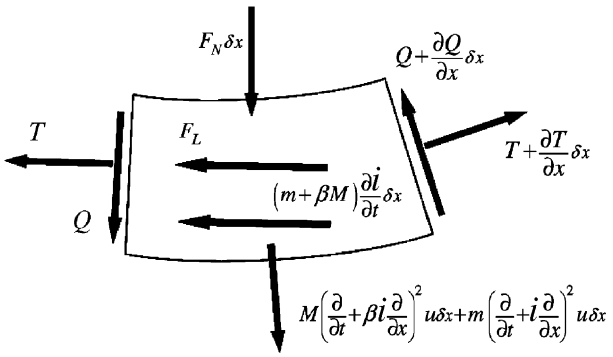

Fig. 2. Equilibrium of forces on a beam element.

Second-order terms involving u have been discarded in Eqs. (5) and (6) because only small transverse displacements are considered. Therefore, the x-direction components of the normal viscous force and the inertia force have been neglected; also, because its effect is of second order, gravity is not considered in this horizontal extension system. Furthermore, by assuming the effects of shear deformation and rotary inertia to be negligible, the shear force can be simplified to

$$Q = -E_0 I \frac{\partial^3 u}{\partial x^3}. \tag{7}$$

2.4. Viscous forces

Ideally, the forces related to the interaction between the cylinder and the fluid should all be computed using the Navier–Stokes equation. Because of the strong dependence on time of the pressure field in the fluid surrounding an oscillatory system, solving the Navier–Stokes equation would be complex and difficult. This is why in this study the interactions between the cylinder and the fluid are calculated in two parts, namely the inviscid forces analytically and the viscous forces semi-empirically. This simplified approach has proven to be successful (Païdoussis [1, Chapters 8 and 9]) for the dynamics of beams in axial flow, a closely similar dynamical system.

The viscous drag acting on the beam can be calculated using the equations derived by Taylor [11]. Those equations were derived to account for the normal and longitudinal components of the force exerted on a long cylinder placed at an angle i in a flow of velocity U. The normal component is divided into parts that correspond to the pressure (form drag) and to the skin friction, while the longitudinal component is solely due to skin friction:

$$F_N = \frac{1}{2}\rho D U^2 (C_D \sin^2 i + C_f \sin i), \tag{8}$$

$$F_L = \frac{1}{2}\rho D U^2 C_f \cos i, \tag{9}$$

where D is the beam diameter, C_D and C_f are, respectively, the form and friction drag coefficients for a cylinder in cross-flow. Here, the relative velocity between the fluid and the beam is exactly equal to $U = (\dot{l}^2 + v^2)^{1/2}$, which is linearized to $U \cong \dot{l}$. Using the same linearization, the angle of incidence i of the flow with a beam element is given by

$$\sin i = \frac{v}{\sqrt{\dot{l}^2 + v^2}} \simeq \frac{v}{\dot{l}}, \quad \cos i = \frac{\dot{l}}{\sqrt{\dot{l}^2 + v^2}} \simeq 1. \tag{10}$$

Substituting Eq. (10) in Eqs. (8) and (9) gives

$$F_N = \frac{1}{2}\rho D[C_D v^2 + C_f \dot{l} v], \tag{11}$$

$$F_L = \frac{1}{2}\rho D \dot{l}^2 C_f. \tag{12}$$

In order to linearize Eq. (11), the least squares approximation is applied over a period of oscillation on the rate of work (power) developed by the friction-drag force, namely the force times the velocity, which gives a constant times the cube of the velocity:

$$v^3 \cong v^2 v_{\max}(8/3\pi). \tag{13}$$

Linearizing by making use of Eq. (13) and substituting u for v using Eq. (2), Eq. (11) becomes

$$F_N = \frac{1}{2}\rho D\left[C_D v_{\max}\frac{8}{3\pi}\left(\frac{\partial u}{\partial t} + \dot{l}\frac{\partial u}{\partial x}\right) + C_f \dot{l}\left(\frac{\partial u}{\partial t} + \dot{l}\frac{\partial u}{\partial x}\right)\right]. \tag{14}$$

Then, substituting in the definition of Eq. (3), Eqs. (12) and (14) become

$$F_N = \frac{1}{2}C_N\left(\frac{M}{D}\right)\dot{l}\left(\frac{\partial u}{\partial t} + \dot{l}\frac{\partial u}{\partial x}\right) + \frac{1}{2}\tilde{C}_N\left(\frac{M}{D}\right)\left(\frac{\partial u}{\partial t} + \dot{l}\frac{\partial u}{\partial x}\right), \tag{15}$$

$$F_L = \frac{1}{2}C_T\left(\frac{M}{D}\right)\dot{l}^2, \tag{16}$$

where

$$C_N = C_T = (4/\pi)C_f, \tag{17}$$

$$\tilde{C}_N = (4/\pi)(8v_{\max}/3\pi)C_D. \tag{18}$$

2.5. Axial tension

In order to find the axial tension in the beam, Eq. (16) is substituted into Eq. (5) and the whole is integrated over x, while the integration constant is replaced by some value of tension at the free end of the beam; i.e.,

$$T(x) = (m + \beta M)\ddot{l}(x - l) + \frac{1}{2}C_T\left(\frac{M}{D}\right)\dot{l}^2(x - l) + T(l). \tag{19}$$

A nonzero value of $T(l)$ may arise from drag-induced compression at the free end, which may be considered proportional to $-\frac{1}{2}\rho\left(\frac{1}{4}\pi D^2\right)\dot{l}^2$, i.e.,

$$T(l) = -\frac{1}{2}\tilde{C}_T M \dot{l}^2, \tag{20}$$

where $\tilde{C}_T$ is a coefficient associated with the form drag at the free end. Substituting Eq. (20) back into Eq. (19), the axial tension in the beam is obtained:

$$T(x) = -\frac{1}{2}C_T\left(\frac{M}{D}\right)\dot{l}^2(l - x) - (m + \beta M)\ddot{l}(l - x) - \frac{1}{2}\tilde{C}_T M \dot{l}^2. \tag{21}$$

In Taleb and Misra's [10] work, the free-end effect is wrongly taken to be a tension (the sign of $T(l)$ is positive).[1]

[1]This is possibly due to the fact that the derivation of the equations of motion in that work was inspired from Païdoussis [12] where the dynamics of a cylinder in axial flow is considered. In that study, the leading edge of the cylinder is clamped and the trailing edge is free: hence a tension is induced by free-end drag. However, in the present study, the free-end drag should really create a compression on the beam.

2.6. Final equation of motion

Substituting Eqs. (7), (15), (16), and (21) into (6), the equation of small lateral motions becomes

$$E_0 I\left(1+\gamma\frac{\partial}{\partial t}\right)\frac{\partial^4 u}{\partial x^4}+\left[(m+M\beta^2)\dot{l}^2+\frac{1}{2}C_T\frac{M}{D}\dot{l}^2(l-x)+(m+\beta M)\ddot{l}(l-x)+\frac{1}{2}\tilde{C}_T M\dot{l}^2\right]\frac{\partial^2 u}{\partial x^2}$$
$$+\left[\frac{1}{2}(C_N\dot{l}+\tilde{C}_N)\dot{l}\frac{M}{D}\right]\frac{\partial u}{\partial x}+(m+\beta M)\dot{l}\left(\frac{\partial^2 u}{\partial x\partial t}+\frac{\partial^2 u}{\partial t\partial x}\right)+(m+M)\left(\frac{\partial^2 u}{\partial t^2}\right)$$
$$+\frac{1}{2}(C_N\dot{l}+\tilde{C}_N)\frac{M}{D}\left(\frac{\partial u}{\partial t}\right)=0. \tag{22}$$

In the limiting case where β is taken to be equal to unity, Eq. (22) differs from Taleb and Misra's [10] equation of motion by three terms. The correction brought in the calculation of the tension in Eq. (21) changes the sign of the free-end drag term, and the addition of the added mass effect in the axial summation of forces of Eq. (5) leads to the addition of the extra term $[\beta M\ddot{l}(l-x)]\partial^2 u/\partial x^2$ and the cancellation of the $\beta M\ddot{l}\,\partial u/\partial x$ term.[2]

3. Analysis

3.1. Series solution

The transverse displacement is expanded in series form, in terms of a set of comparison functions:

$$u(x,t)=\sum_{n=1}^{\infty}\phi_n(x,l)f_n(t). \tag{23}$$

The comparison functions $\phi_n(x,l)$ can be somewhat arbitrary, as long as they satisfy the boundary conditions. In the present analysis, the cantilevered beam eigenfunctions are utilized:

$$\phi_n(x,l)=[\cosh(\lambda_n x/l)-\cos(\lambda_n x/l)]-\sigma_n\left[\sinh(\lambda_n x/l)-\sin(\lambda_n x/l)\right], \tag{24}$$

where

$$\sigma_n=(\cosh\,\lambda_n+\cos\,\lambda_n)/(\sinh\lambda_n+\sin\,\lambda_n) \tag{25}$$

and λ_n are the eigenvalues given by the roots of the transcendental equation

$$1+\cosh\lambda_n\cos\,\lambda_n=0 \tag{26}$$

as given in Bishop and Johnson [13].

Substituting the series solution of Eq. (23) into Eq. (22) and applying Galerkin's procedure, after some manipulation the equation of motion becomes

$$\ddot{f}_s=\sum_{n=1}^{\infty}\left[\left\{-E_0 I\gamma\frac{\lambda_n^4}{(M+m)l^4}-\frac{1}{2}(C_N\dot{l}+\tilde{C}_N)\frac{M}{D(M+m)}\right\}\delta_{ns}-2\frac{\dot{l}}{l}\frac{m+\beta M}{m+M}a_{ns}+2\frac{\dot{l}}{l}c_{ns}\right]\dot{f}_n$$
$$+\left[\left\{E_0 I\gamma\frac{\lambda_n^4}{(M+m)l^5}\dot{l}+\frac{\ddot{l}}{l}-2\frac{\dot{l}^2}{l^2}+\frac{1}{2}\frac{M}{D(M+m)}\frac{\dot{l}}{l}(C_N\dot{l}+\tilde{C}_N)\right\}c_{ns}\right.$$
$$\left.+\left\{\frac{m+\beta M}{M+m}\frac{\ddot{l}}{l}+\frac{1}{2}C_T\frac{M}{M+m}\frac{\dot{l}^2}{lD}+2\frac{\dot{l}^2}{l^2}\frac{m+\beta M}{m+M}\right\}d_{ns}-\frac{\dot{l}^2}{l^2}e_{ns}\right.$$

[2]The authors of the present paper have also found a number of algebraic and typographic errors in the Taleb and Misra [10] paper; see Appendix A.

$$-E_0 I\delta_{ns}\frac{\lambda_n^4}{(M+m)l^4}+E_0 I\delta_{ns}\frac{4\gamma\dot{l}\lambda_n^4}{(M+m)l^5}+\left\{-\frac{1}{2}(C_N\dot{l}+\tilde{C}_N)\frac{M}{(M+m)D}\frac{\dot{l}}{l}+2\frac{m+\beta M}{m+M}\frac{\dot{l}^2}{l^2}\right\}a_{ns}$$
$$-\left\{\frac{1}{2}\left[C_T\frac{l}{D}+\tilde{C}_T\right]\left[\frac{M}{M+m}\right]\left(\frac{\dot{l}}{l}\right)^2+\frac{m+\beta^2 M}{m+M}\left(\frac{\dot{l}}{l}\right)^2+\frac{m+\beta M}{M+m}\frac{\ddot{l}}{l}\right\}b_{ns}\Bigg]f_n\quad(s=1,2,\ldots\infty), \tag{27}$$

where δ_{ns} is the Kronecker delta and

$$a_{ns}=\int_0^l\frac{\partial\phi_n}{\partial x}\phi_s\,\mathrm{d}x,\quad b_{ns}=l\int_0^l\frac{\partial^2\phi_n}{\partial x^2}\phi_s\,\mathrm{d}x,\quad c_{ns}=\frac{1}{l}\int_0^l x\frac{\partial\phi_n}{\partial x}\phi_s\,\mathrm{d}x,$$
$$d_{ns}=\int_0^l x\frac{\partial^2\phi_n}{\partial x^2}\phi_s\,\mathrm{d}x,\quad e_{ns}=\frac{1}{l}\int_0^l x^2\frac{\partial^2\phi_n}{\partial x^2}\phi_s\,\mathrm{d}x. \tag{28}$$

The way to find numerical values for Eqs. (28) is explained in Appendix B.

3.2. Non-dimensionalization

It is convenient to describe the dynamics in terms of dimensionless quantities by defining

$$\tau=t\left[\frac{E_0 I}{(M+m)l_0^4}\right]^{1/2}=\alpha t,\ R=\frac{l}{l_0},\ \varepsilon=\frac{l_0}{D},\ \Gamma=\frac{m}{M},\ \bar{\gamma}=\gamma\alpha,\ \overline{C}_N=\frac{\tilde{C}_N}{\alpha l_0},\ \psi=\frac{M}{m+M} \tag{29}$$

and

$$f_s(t)=F_s(\tau),\quad \dot{f}_s(t)=\alpha\dot{F}_s(\tau),\quad \ddot{f}_s(t)=\alpha^2\ddot{F}_s(\tau),$$
$$l(t)=l_0R(\tau),\quad \dot{l}(t)=l_0\alpha\dot{R}(\tau),\quad \ddot{l}(t)=l_0\alpha^2\ddot{R}(\tau), \tag{30}$$

where l_0 is the original length of the beam. When placed over a dimensional quantity, the dot means the derivative with respect to time, and when it is placed over a dimensionless quantity, it means the derivative with respect to non-dimensional time. Introducing the dimensionless quantities into Eq. (27), we obtain

$$\ddot{F}_s=\sum_{n=1}^{\infty}\Bigg[\left\{-\frac{\lambda_n^4\bar{\gamma}}{R^4}-\frac{1}{2}(C_N\dot{R}+\bar{C}_N)\psi\varepsilon\right\}\delta_{ns}-2\frac{\dot{R}}{R}\psi(\Gamma+\beta)a_{ns}+2\frac{\dot{R}}{R}c_{ns}\Bigg]\dot{F}_n$$
$$+\Bigg[\left\{\frac{\lambda_n^4\bar{\gamma}\dot{R}}{R^5}+\frac{\ddot{R}}{R}-2\frac{\dot{R}^2}{R^2}+\frac{1}{2}\psi\varepsilon\frac{\dot{R}}{R}(C_N\dot{R}+\bar{C}_N)\right\}c_{ns}+\left\{(\Gamma+\beta)\psi\frac{\ddot{R}}{R}+\frac{1}{2}C_T\psi\frac{\dot{R}^2\varepsilon}{R}+2\frac{\dot{R}^2}{R^2}\psi(\Gamma+\beta)\right\}d_{ns}$$
$$-\left\{\frac{\dot{R}^2}{R^2}\right\}e_{ns}+\left\{-\frac{\lambda_n^4}{R^4}+4\bar{\gamma}\frac{\dot{R}}{R^5}\lambda_n^4\right\}\delta_{ns}+\left\{-\frac{1}{2}(C_N\dot{R}+\bar{C}_N)\psi\varepsilon\frac{\dot{R}}{R}+2\psi\frac{\dot{R}^2}{R^2}(\Gamma+\beta)\right\}a_{ns}$$
$$-\left\{\frac{1}{2}[C_TR\varepsilon+\tilde{C}_T]\psi\frac{\dot{R}^2}{R^2}+\psi(\Gamma+\beta^2)\frac{\dot{R}^2}{R^2}+(\Gamma+\beta)\psi\frac{\ddot{R}}{R}\right\}b_{ns}\Bigg]F_n\quad(s=1,2,\ldots\infty). \tag{31}$$

3.3. Computational analysis

After truncation of the summation in Eq. (31) at $n=4$, it is integrated using a Runge–Kutta algorithm with error control for systems of equations. This algorithm is the ode45 function from the Matlab software. Calculations have been performed with the values of some parameters of the system fixed, as given in Table 1.

Table 1
Values of the parameters kept constant in the calculations

Parameters	$\bar{\gamma}$	ψ	ε	C_N	$\bar{C}_N$	C_T	$\bar{C}_T$
Values	0	0.5	1	1	0.1	1	1

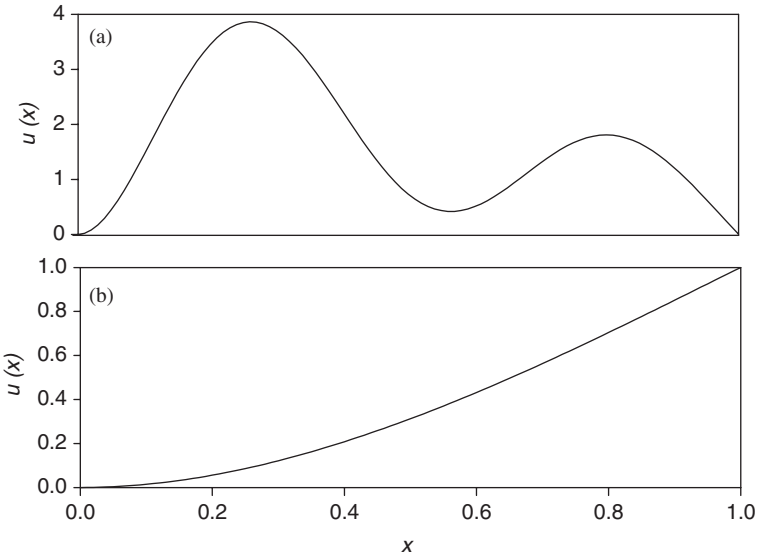

Fig. 3. (a) Initial displacement of the beam in Taleb and Misra [10]. (b) Realistic initial displacement of the beam used in this paper.

Table 2
Realistic initial conditions of the beam as used in the calculations

Mode (N)	$F_N(0)$	$\dot{F}_N(0)$
1	0.4855	0
2	−0.01246	0
3	0.001676	0
4	−0.0004011	0

3.4. Initial conditions

In the paper by Taleb and Misra [10], the initial conditions are unitary for the four generalized displacements F_n, while all first non-dimensional time derivatives are nil. This leads to quite an awkward initial shape for the beam as seen on Fig. 3(a), which is not representative of what could easily be done in an experiment.

If a load P is applied at the tip of a Euler cantilever beam, the displacement has the form $u = (P/EI)(x^2/2 - x^3/6)$. In that train of thought, a curve fit is done using the beam eigenfunctions for the displacement $u = 3x^2/2 - x^3/2$, which gives a tip displacement of 1 for a beam of length 1. The resulting initial displacement is shown on Fig. 3(b) and the corresponding initial conditions can be found in Table 2. The initial conditions are used for the computations where the physical displacement of the beam is sought. For modal analysis, the initial conditions are unitary for all four generalized displacements F_n.

It has to be emphasized that this study is linear; therefore the tip displacement of the beam is linearly proportional to its initial displacement, and there is no scaling factor between the extension rate and the transverse displacement. It is only a matter of initial conditions.

4. Results and discussion

Results are obtained for different cases of extension rates, namely constant rates and trapezoidal deployment rate profiles. Emphasis is put into understanding the effect of viscous forces acting on the system, as well as the mechanism for static instability.

In an attempt to reproduce the results published by Taleb and Misra [10], the dynamics of the system is computed for the case of a free-end tension ($\tilde{C}_T = -1$). The plots of the dynamics of the beam for such conditions are shown in Fig. 4. The plots are almost identical to those published by Taleb and Misra [10]. The slight discrepancies come from the differences in the equations of motion mentioned in Section 2.6. For the sake of comparison, the behaviour of the beam is plotted for the case of free-end compression in Fig. 5. We notice, by comparison to Fig. 4, that the amplitude of the system subjected to a free-end compression is larger. This is due to the diminution in stiffness due to the compression, as intuitively expected.

4.1. Constant extension rate

4.1.1. Dynamics and stability of constant extension deployment

The dynamical behaviour of the beam during uniform extension is illustrated in Fig. 6. For each value of the extension rate, two graphs are plotted: on the left-hand side, the tip displacement is plotted against time to show the dynamics of the system; and on the right-hand side, the tip displacement over the instantaneous non-dimensional length of the beam is plotted against time to highlight the development of instability. The dependence of non-dimensional length of the beam, $R(\tau)$, on non-dimensional time is indicated in the caption.

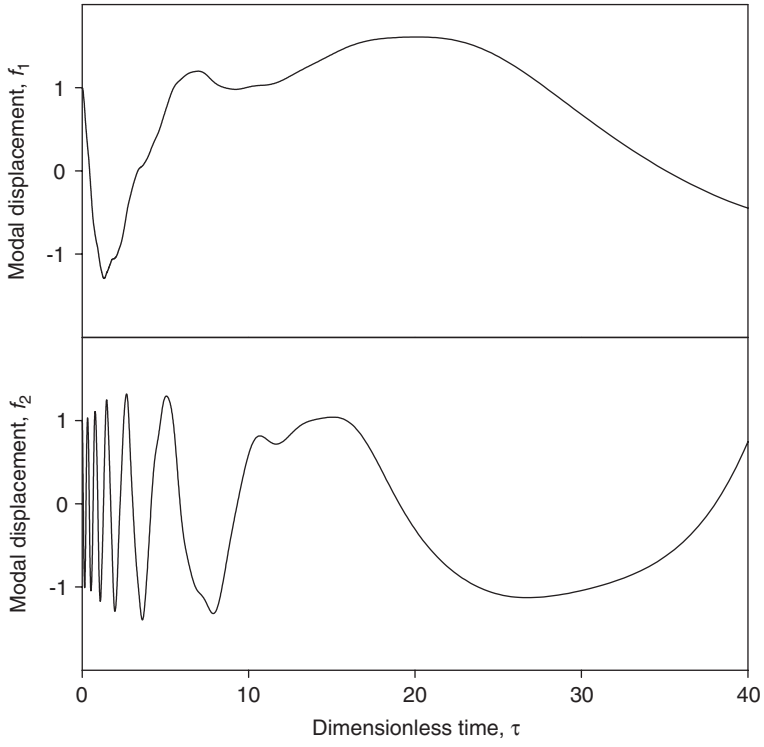

Fig. 4. Dynamical behaviour of the beam during uniform extension with a tension applied at the free end ($\tilde{C}_T = -1$) for a system with $\dot{R} = 0.5$ and $\beta = 1$.

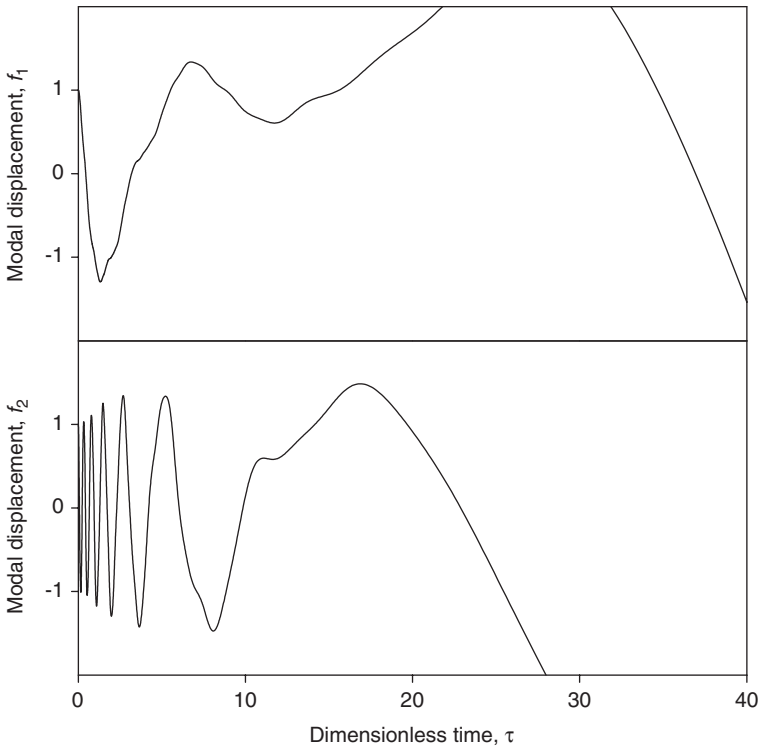

Fig. 5. Dynamical behaviour of the beam during uniform extension with the correct compression applied at the free end ($\tilde{C}_T = 1$) for a system with $\dot{R} = 0.5$ and $\beta = 1$.

The parameters kept constant are given in Table 1. The coefficient of axial added mass (β) is also kept constant on all graphs of Fig. 6; it is arbitrarily given a value of 1/3, which could be considered quite high.

For extension rates slower than 0.3 the behaviour of the beam during the extrusion process is characterized by a phase of oscillation with increasing amplitude and decreasing frequency (see Fig. 6(a)–(f)). This is as expected; as the beam lengthens, the mass of the system increases and the stiffness decreases. Hence, the stiffness to mass ratio decreases even faster, which causes the frequencies of oscillation to diminish and the amplitude to increase. As the beam keeps lengthening, the frequencies decrease even further, and the motion seems to become heavily damped. The amplitude keeps decreasing until the beam has very small lateral motion. However, as the beam lengthens even more, it becomes more and more flimsy and eventually becomes statically unstable; divergence is clearly seen in Fig. 6(b,d,f,h).

For faster extension rates, such as in Fig. 6(g), the frequencies of oscillation decrease even faster and the amplitude of the displacement increases rapidly until divergence. In this case, the system does not exhibit a heavy damping phase.

Because of the complexity of its behaviour and because of the fact that the system changes with time (i.e., the length of the beam increases), some instability phenomena are not necessarily obvious from the tip displacement plots. The evolution in time of the frequencies and the damping of the beam offer a deeper insight into the mathematical nature of the stability of the system. Of course, an eigenvalue analysis of an equation involving time-varying terms may be considered to be meaningless. Nevertheless, adopting a ''quasi-static'' viewpoint, the instantaneous eigenvalues may be used to gain some additional insight, even though they can at best only approximate the dynamics of the actual system. The dimensionless frequencies, Re(ω), and damping, Im(ω), are plotted versus time for the extension rates of $\dot{R} = 0.25$ in Fig. 7. The letters in the plots (A–D) allow matching the loci of the frequencies of oscillation of the system with the corresponding damping loci. It must be kept in mind that the different frequencies of oscillation of the system differ from the

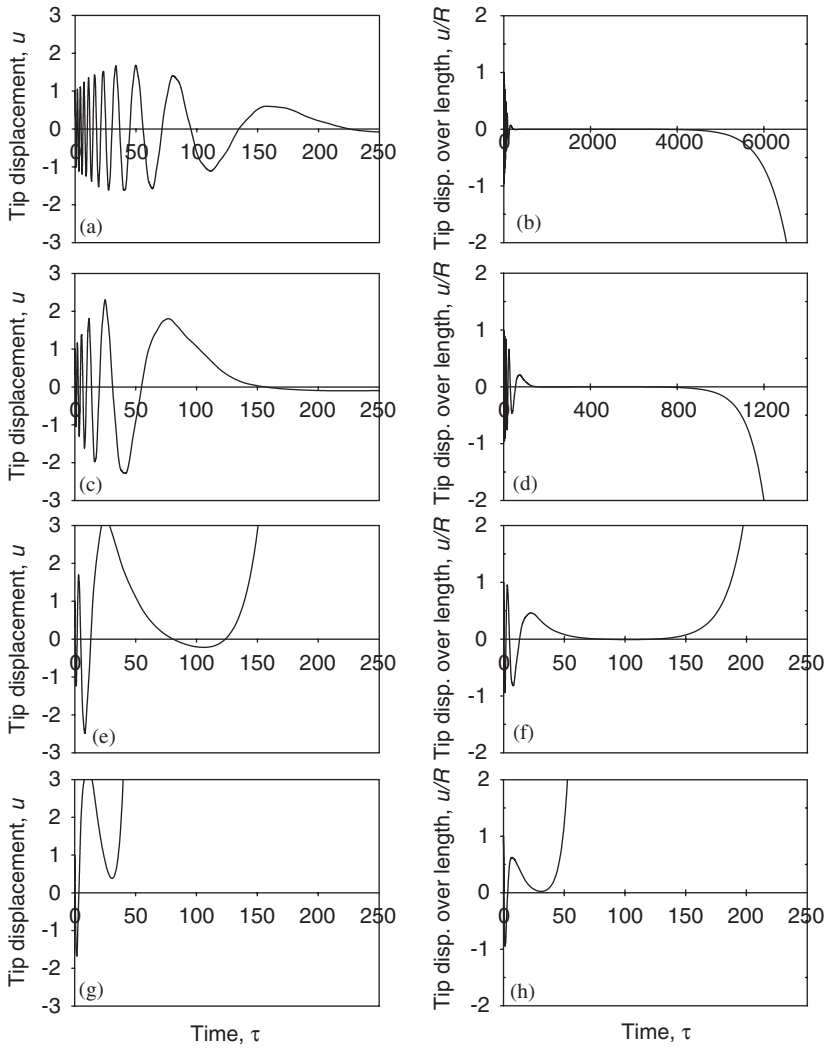

Fig. 6. Behaviour of the beam during uniform extension depending on the extension rate: (a), (b) $\dot{R} = 0.05$; (c), (d) $\dot{R} = 0.1$; (e), (f) $\dot{R} = 0.25$; (g, h) $\dot{R} = 0.5$; $\beta = 1/3$ throughout.

four classical beam modes in this four-mode calculation; the extrusion and the viscous forces cause the coupling of these modes.

The dimensionless frequencies of oscillation of the system diminish rapidly in the first part of the deployment. The plot of Fig. 7(a) does not show the frequencies in this early phase as they are, at time zero, several orders of magnitude greater than the range of the graph. In this early phase, we can see from Fig. 7(b) that the system is damped until dimensionless time of $\tau = 54$, where mode B loses stability through what would seem like flutter instability ($\mathrm{Re}(\omega) > 0$ and $\mathrm{Im}(\omega) < 0$). One notices though that the corresponding instantaneous period of oscillation of mode B, $T = 2\pi/\mathrm{Re}(\omega)$, at time $\tau = 54$ is approximately 143. Add to this the fact that the period is increasing with time faster than the oscillation is happening, i.e. $\mathrm{d}T/\mathrm{d}\tau > 1$, and it is clear that no physical oscillation is really happening. So, the loss of stability shown in Fig. 7 is really a static instability.

By looking at Fig. 6(f), we can estimate that the beam extending at a rate of $\dot{R} = 0.25$ starts diverging at a time of about 150, while in Fig. 7(b) we can clearly see that the system is unstable from time $\tau = 54$ on. The discrepancy between these values can be explained by looking at Fig. 8 where the entire shape of the beam is plotted at different instants during the development of instability. From this figure it is obvious that in the

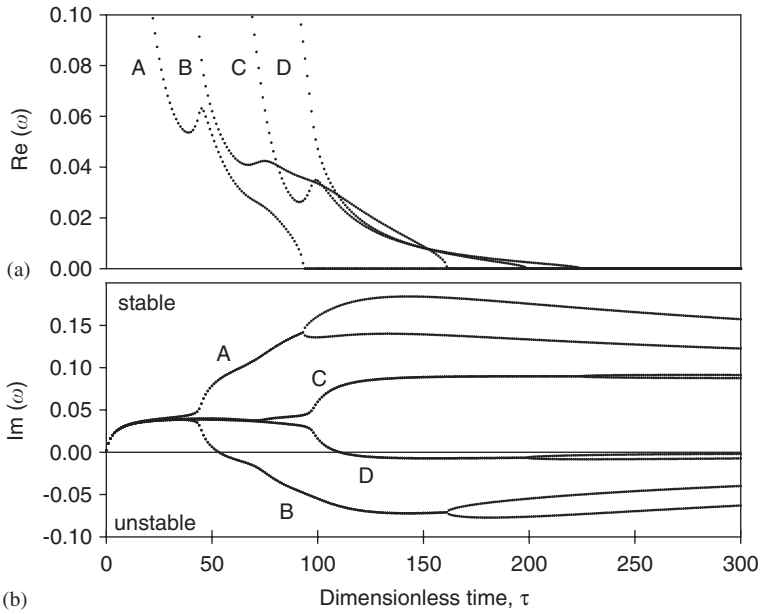

Fig. 7. Evolution in time of the frequencies (a) and damping (b) of the system at constant extension rate $\dot{R} = 0.25$ for $\beta = 1/3$. The letters A–D allow to match the frequencies with their respective damping.

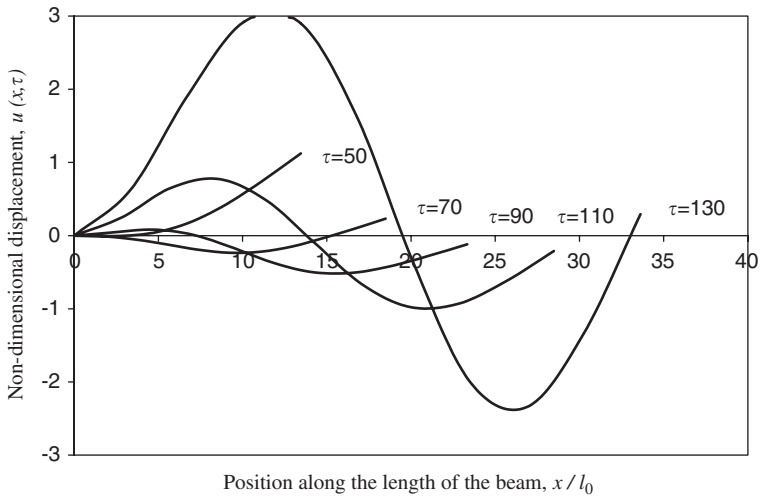

Fig. 8. Complete shape of the beam during the onset of instability at an extension rate of $\dot{R} = 0.25$ and $\beta = 1/3$.

course of development of instability, the tip of the beam barely moves. In this instability, the motion of the beam is dominated by mode B, the maximum displacement occurring at about 40% of the length, whereas the tip has little displacement. Moreover, from Fig. 7, it is seen that for $\tau = 160$, mode B becomes statically unstable ($\mathrm{Re}(\omega) = 0$ and $\mathrm{Im}(\omega)$ bifurcates).

If we rely on the quasi-static analysis of the instantaneous frequencies and damping, such as the one presented in Fig. 7, some conclusions can be drawn. For any extension rate slower than 0.3, the instantaneous frequencies of oscillation decrease until static instability is reached. For extension rates equal to or greater than 0.3, the system is actually unstable from the very beginning of the deployment, as the system flutters in all its modes. But after a few oscillations, the system regains stability as its length increases, but it loses stability again, but this time through buckling. For extension rates equal or faster than 2.97, the beam is unstable for

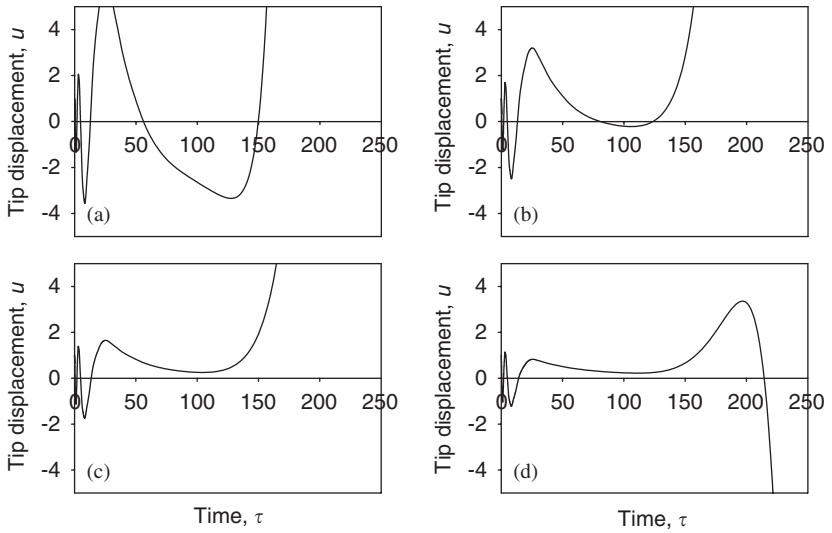

Fig. 9. Behaviour of the beam during uniform extension depending on the axial added mass coefficient for $\dot{R} = 0.25$: (a) $\beta = 0$; (b) $\beta = 1/3$; (c) $\beta = 2/3$; (d) $\beta = 1$.

the entire deployment. From the very beginning of the extension process, all modes are fluttering, although modes A, C, D regain stability as the beam lengthens, while mode B flutters until it diverges statically.

4.1.2. Effect of the axial added mass coefficient

The dynamical behaviour of the beam is plotted in Fig. 9 for different values of the coefficient of axial added mass, β. Here, a legitimate question to ask is what is a physically reasonable value for β. Clearly, this depends on the surface roughness and chemical composition of the deploying beam and the fluid, possible electrodynamic effects, as well as to what extent the boundary layer remains attached in the course of deployment and lateral motions. Although a definite answer to this question would require further study and experimental validation, it may be said that $\beta = 1/3$ is likely an upper limit, with physically reasonable values in the range of $\beta = 0 - 0.2$. Hence, the values of $\beta = 2/3$ and $\beta = 1$ are unrealistically high, but they are used to exaggerate the effect of β to study it more easily.

As seen in Fig. 9, the most important effect of this coefficient on the dynamics of the system occurs in the course of early deployment. The amplitude increase is much steeper for smaller values of β, and almost no amplitude increase takes place early in the deployment when $\beta = 1$. This was expected because, if more inertia is added to the system (larger β), the amplitude should be smaller. The coefficient β does play a small role in the stability of the system later in the extrusion by delaying a little the static instability as the coefficient is increased. It is true that the effect of β on the stability of the system is much less than that of the deployment rate.

Once again, for a deeper understanding of the mathematical nature of the stability of the system, we turn our attention to plots of the evolution in time of the frequencies and the damping of the system. They are presented in Figs. 10 and 11 for values of β of 0 and 1 in the case of an extension rate of $\dot{R} = 0.25$. The effect of β on the stability of the system becomes obvious by comparing the damping in early deployment in Figs. 10(b) and 11(b). We can notice that for a large value of β (Fig. 11(b)) the system is stable early in the deployment, while for a small value of β (Fig. 10(b)) the system flutters. This explains why in Fig. 9(a) the increase in amplitude is so much steeper than for larger values of β: in this case the system gains amplitude not only through softening of the stiffness but mostly because it is dynamically unstable. Also, as it was noticed in Fig. 9, the coefficient of axial added mass does play a small role in delaying the static instability. We can see that in Fig. 10(b) divergence occurs when the damping of mode A crosses the zero-damping axis at time $\tau = 47$ for $\beta = 0$, and in Fig. 11(b) mode B crosses the zero-damping axis at time $\tau = 65$ for $\beta = 1$.

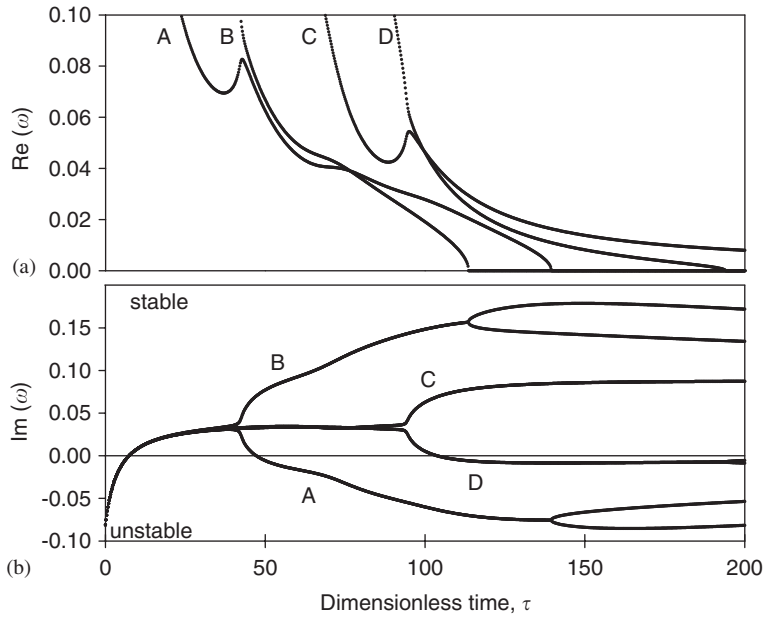

Fig. 10. Evolution in time of the frequencies and damping of the system at constant extension rate $\dot{R} = 0.25$ for $\beta = 0$.

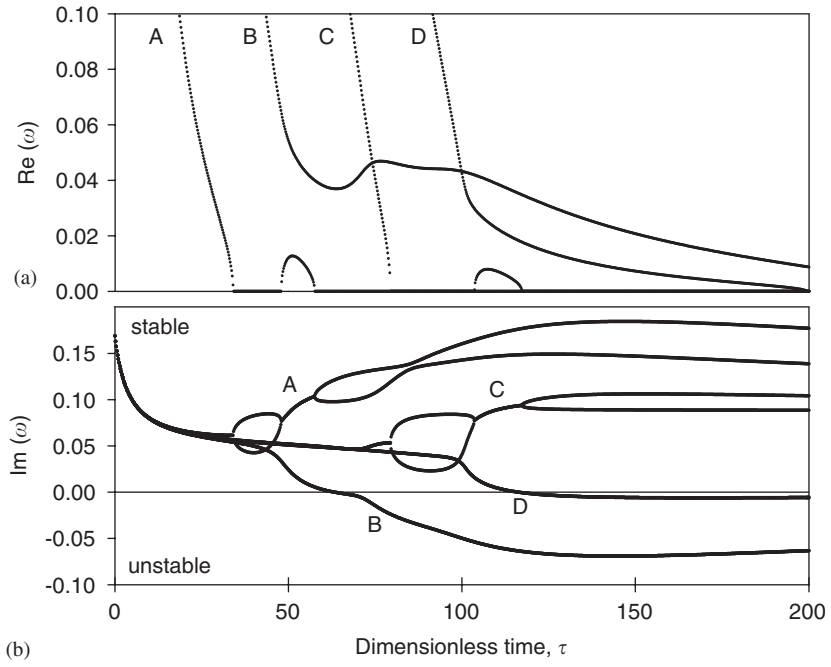

Fig. 11. Evolution in time of the frequencies and damping of the system at constant extension rate $\dot{R} = 0.25$ for $\beta = 1$.

These findings relate to a similar effect observed in the dynamics of travelling web (Païdoussis [1, pp. 1207–1213]). However, in the case of travelling web, the effect of the added mass on the dynamics is much more significant than for extruding beams.

4.2. Trapezoidal velocity profile deployment

4.2.1. Dynamics and stability of trapezoidal velocity profile deployment

In the trapezoidal velocity profile deployment, the beam first accelerates at a constant rate, then deploys at its cruise speed, and finally decelerates and stops as the wanted final length is reached, as shown on Fig. 12. This would be representative of real-life deployment scenarios because the beam stops deploying at a given length, rather than continue extending until instability is reached.

The dynamical behaviour of the beam during trapezoidal velocity profile extension is illustrated in Fig. 13. A maximum amplitude plot is presented in Fig. 14. The profile studied here is "5-90-5", meaning that 5% of the deployment time is spent in the acceleration phase, 90% in the cruise-speed phase, and 5% in the deceleration phase. The tip displacement is plotted for several values of deployment time necessary to reach a length 20 times the original one. The dashed lines in Fig. 13 represent the change of deployment phase in the velocity profile.

For long deployment time, as in Fig. 13(a) and (b), the dynamical behaviour is very similar to that of constant extension rate deployment: the faster the beam travels, the larger the transverse movement can become. On the other hand, for shorter deployment rates, the phase of deceleration and the complete stop

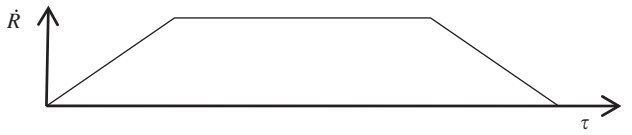

Fig. 12. Variation of the deployment rate with time during a trapezoidal velocity profile deployment.

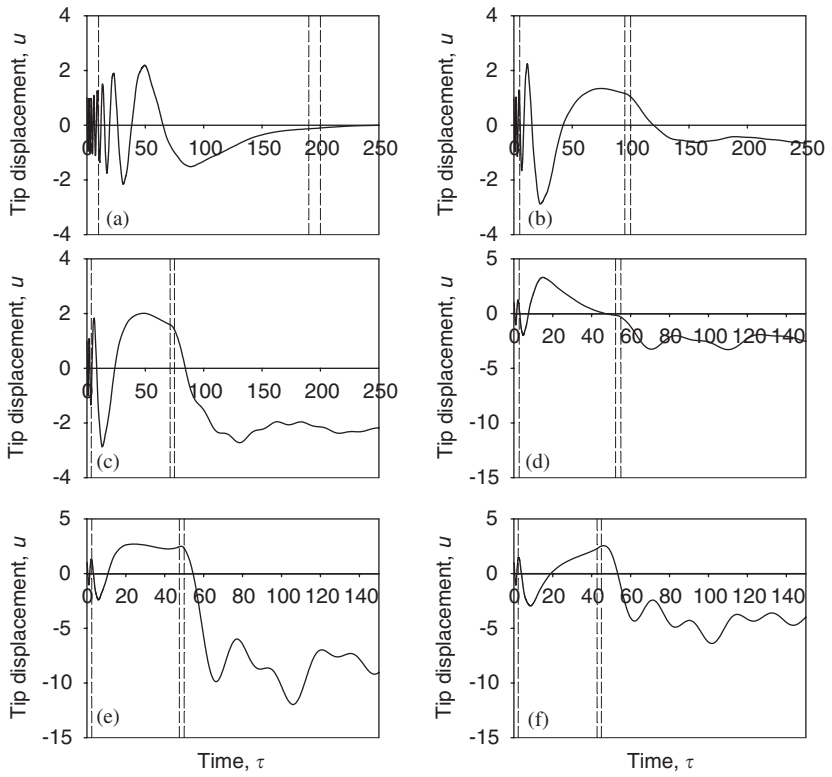

Fig. 13. Behaviour of the beam during trapezoidal velocity profile extension depending on the deployment time, 5-90-5 profile with $R_f = 20$ and $R_0 = 1$ for $\beta = 1/3$ and (a) $\tau_f = 200$; (b) $\tau_f = 100$; (c) $\tau_f = 75$; (d) $\tau_f = 55$; (e) $\tau_f = 50$; (f) $\tau_f = 45$.

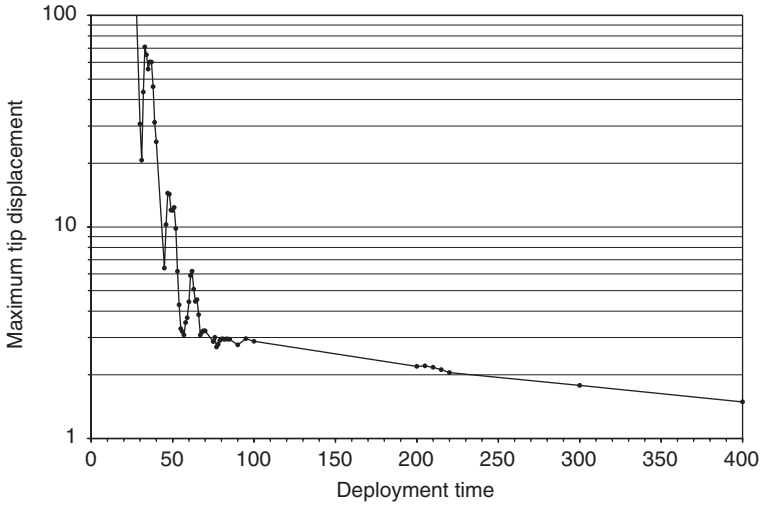

Fig. 14. Maximum amplitude of oscillation of 5-90-5 trapezoidal deployment depending on the deployment time, $R_f = 20$, $\beta = 1/3$.

really do have an important effect on the dynamics of the system. In Fig. 13(e) and (f), the curves of the tip displacement bend abruptly during the deceleration phase or just after the deployment stopped.

It is obvious that once the beam has stopped deploying it is stable, because the system is now autonomous and the only external force acting on it is the transverse viscous damping. But then why is it that the maximum amplitude of oscillation during trapezoidal deployment is observed *after* the beam has stopped extruding? This can be explained by the reorganization of the instantaneous eigenmodes of the system and the significant increase of the instantaneous frequencies of oscillation due to the elimination of the axial velocity of the beam. The extension rate of the beam influences the effective rigidity of the system through the centrifugal force, the Coriolis force and the compression of the beam. During deployment, these forces tend to reduce the frequencies of oscillation. The extension rate is also responsible for a significant source of damping via the transverse viscous forces, the Coriolis force and the d'Alembert forces (inertia forces). So, when the beam stops deploying, the instantaneous eigenmodes of vibration and the frequencies of oscillation completely change. If we look back at Fig. 7(a) for a constant extension rate deployment, we see that the frequencies of the system drop quite rapidly during the early phase of the deployment. The same thing applies with the trapezoidal velocity profile deployment: when the beam has reached a certain length, the extension rate keeps the instantaneous frequencies of oscillation very small through the aforementioned forces, but when that extension rate is reduced to zero, the system releases its accumulated energy by oscillating as a simple cantilevered beam of constant length in dense fluid.

On the plots of Fig. 13(b)–(e), the tip of the beam seems to be oscillating about an equilibrium point located off the abscissa. This observation is perplexing, because a priori there is no force, which could hold the beam down or up. The only possible explanation is that the beam is moving extremely slowly through the viscous fluid, as a spoon passing through cold molasses. This phenomenon motivates a deeper study of the viscous forces acting on the beam, which is done in the next section.

From inspection of Fig. 13, there is a general trend for the amplitude of oscillation to grow as the deployment time is reduced. But there seems to be an exception when moving from plots (d) to (e). As the deployment time falls from 55 to 50, the amplitude decreases significantly. Other similar cases are recorded for deployment times of 33, and 57, where the amplitude is larger than at a slightly faster or slower deployment rates. These amplitude peaks for certain deployment rates, shown on Fig. 14, were first thought to be due to a resonance phenomenon related to flexural travelling waves (Gosselin [14]). Further investigation quickly proved those peaks to be random and due to initial conditions. The maximum amplitude plot of Fig. 14 corresponds to the initial conditions described in Section 3.4. Using a different set of initial conditions, the maximum amplitude peaks occur at different deployment times, but the general curve for the maximum amplitude is of sensibly the same shape.

Table 3
Viscously damped free vibration of the four modes

Mode, s	1	2	3	4
Damping ratio, ζ_s	1.422	0.227	0.081	0.041

4.3. Effects of the viscous forces on the system

In the previous section, perplexing plots (Fig. 13(b)–(e)) were presented of the tip of the beam seemingly oscillating about an equilibrium point off the axis of stable equilibrium; also the key role that damping plays in the stability of the beam was remarked upon. These considerations provided the motivation for the quest for a deeper understanding of the effects of the viscous forces on the behaviour of the system. In order to do so, it seems appropriate to simplify the system to one of a constant-length beam oscillating in a dense fluid. Analysing the equation of motion of this simplified model helps us to understand how the viscous damping is different for the different modes of the system.

For the case of constant length, the equation of motion of the system, Eq. (31), simplifies to

$$\ddot{F}_s + \left(\frac{\lambda_s^4 \bar{\gamma}}{R^4} + \frac{1}{2}\bar{C}_N \psi \varepsilon\right)\dot{F}_s + \frac{\lambda_s^4}{R^4} F_s = 0.$$

In the case studied here, there is no structural damping ($\bar{\gamma} = 0$) and the damping ratio is

$$\zeta_s = \frac{R^2 \bar{C}_N \psi \varepsilon}{4\lambda_s^2}.$$

It is now evident that viscous damping is inversely proportional to the square of the eigenvalue. For a dimensionless length of $R = 20$ and using the eigenvalues of a cantilevered beam, the value of damping ratio is found for each mode and given in Table 3. Recall that for a damping ratio of more that unity, the movement is overdamped, and for a damping ratio of less than unity, the movement is underdamped. At a non-dimensional length of 20, the first mode is therefore overdamped, while the other three are underdamped. Thus, the viscous damping acts in the inverse manner compared to structural damping: viscous damping acts more heavily on lower modes while structural damping acts more heavily on higher modes.

Knowing that the first mode is overdamped, we can confirm the earlier explanation of the behaviour of the beam oscillating about a point off the axis in Fig. 13(b)–(e). The first mode being overdamped, the beam returns to its equilibrium position really slowly through the viscous fluid, exactly as in the analogy of the spoon passing through cold molasses.

The analysis of the simplified equations of motion for the case of constant length confirms that the case where the beam seems to be oscillating about a point off the abscissa is a consequence of the effects of the viscous forces on the dynamics of the system.

5. Conclusion

The equations of motion of a flexible slender cantilevered beam with uniform circular cross-section, extending axially in a horizontal plane at a known rate while immersed in a dense incompressible fluid were derived. An axial added mass coefficient was introduced in these equations in order to better approximate the mass of fluid which stays attached to the oscillating beam while moving in the axial direction. Realistic initial conditions were given to the system and numerical solutions were obtained. The dynamical behaviour of the system was illustrated for cases of constant extension rate and for a trapezoidal deployment rate profile.

In the case of relatively low constant extension rates, the system displays a phase of decaying oscillation with increasing amplitude and decreasing frequency, until the movement is strongly damped and later becomes statically unstable. For faster deployment rates, the beam has a short flutter phase at the beginning of the deployment, followed by a brief phase of damped oscillation until it exhibits static divergence. For fast enough deployment rates, the system is unstable from the beginning and it never restabilizes.

The effect the axial added mass coefficient has on the system was studied. This coefficient plays two roles in the stability of the system: (i) for a very small value of the coefficient, the system can flutter early in the deployment, and (ii) for larger values of the coefficient the onset of static instability is slightly delayed.

The trapezoidal deployment rate profile was studied because it is deemed more representative of real-life applications, in the sense that the beam stops deploying at a given length rather than continue extruding indefinitely or until instability is reached. For long deployment times, the system behaves in a very similar manner to one with low constant extension rate, except that it does not become statically unstable. For shorter deployment times, the maximum amplitude of the tip displacement is usually attained after the beam has stopped extruding. It is also noticed that for certain short extension times, the beam seems to oscillate about a point off the undeformed equilibrium. This is shown to be due to the viscous damping acting on the first mode of the system.

Acknowledgements

The authors are grateful to NSERC (the Natural Sciences and Engineering Research Council of Canada) for funding this research. The first author would like to thank the group of students from the Fluid–Structure Interaction laboratory for moral support during the duration of this research.

Appendix A. Revision of Taleb and Misra [10]

As mentioned in Section 2.6, it came to the attention of the first author (Gosselin [14]) that a few algebraic or typographical errors are present in the paper by Taleb and Misra [10], in addition to the sign error concerning the free-end drag.

Eq. (10) in Taleb and Misra [10] should read

$$
\begin{aligned}
\ddot{f}_s = \sum_{n=1}^{\infty} -\Bigg[& \left\{ E_0 I \gamma \frac{\lambda_n^4}{(M+m)l^4} + \frac{1}{2}(C_N \dot{l} + \tilde{C}_N) \frac{M}{D(M+m)} \right\} \delta_{ns} + 2\frac{\dot{l}}{l}(a_{ns} - c_{ns}) \Bigg] \dot{f}_n \\
& + \left[\left\{ E_0 I \gamma \frac{\lambda_n^4}{(M+m)l^5} \dot{l} + \frac{\ddot{l}}{l} - \boxed{2\frac{\dot{l}^2}{l^2}} + \frac{1}{2} \frac{M}{D(M+m)} \frac{\dot{l}}{l} (C_N \dot{l} + \tilde{C}_N) \right\} c_{ns} \right. \\
& + \left\{ \boxed{\frac{m}{M+m} \frac{\ddot{l}}{l}} + \frac{1}{2} C_T \frac{M}{M+m} \frac{\dot{l}^2}{lD} + 2\frac{\dot{l}^2}{l^2} \right\} d_{ns} - \frac{\dot{l}^2}{l^2} e_{ns} - E_0 I \delta_{ns} \frac{\lambda_n^4}{(M+m)l^4} \\
& + \boxed{E_0 I \delta_{ns} \frac{4\gamma \dot{l} \lambda_n^4}{(M+m)l^5}} \boxed{-} \left\{ \frac{1}{2}(C_N \dot{l} + \tilde{C}_N) \frac{M}{(M+m)D} \frac{\dot{l}}{l} - \boxed{2\frac{\dot{l}^2}{l^2}} + \frac{M}{M+m} \frac{\ddot{l}}{l} \right\} a_{ns} \\
& \left. - \left\{ \frac{1}{2} \left[C_T \frac{l}{D} \boxed{+} \tilde{C}_T \right] \left[\frac{M}{M+m} \right] \left(\frac{\dot{l}}{l} \right)^2 + \left(\frac{\dot{l}}{l} \right)^2 + \frac{m}{M+m} \frac{\ddot{l}}{l} \right\} b_{ns} \right] f_n \quad (s = 1, 2, \ldots \infty),
\end{aligned}
\tag{32}
$$

where the discrepancies between Eq. (32) and the one published previously [10] are boxed.

Table 4
The constants a_{ns}, b_{ns}, c_{ns}, and d_{ns} for a cantilevered beam

Constant	Analytical expression
$a_{ns}(n\neq s)$	$\dfrac{4}{(\lambda_s/\lambda_n)^2+(-1)^{n+s}}$
a_{ss}	2
$b_{ns}(n\neq s)$	$\dfrac{4(\lambda_n\sigma_n-\lambda_s\sigma_s)}{(-1)^{n+s}-(\lambda_s/\lambda_n)^2}$
b_{ss}	$\lambda_s\sigma_s(2-\lambda_s\sigma_s)$
$c_{ns}(n\neq s)$	$\dfrac{4\lambda_n^4(-1)^{n+s}}{\lambda_n^4-\lambda_s^4}$
c_{ss}	$\dfrac{1}{2}(\sigma_s^2-1)$
$d_{ns}(n\neq s)$	$\dfrac{4(\lambda_n\sigma_n-\lambda_s\sigma_s+2)}{1-(\lambda_s/\lambda_n)^4}(-1)^{n+s}-\dfrac{3+(\lambda_s/\lambda_n)^4}{1-(\lambda_s/\lambda_n)^4}\,a_{ns}$
d_{ss}	$\dfrac{1}{2}b_{ss}$

Eq. (13) in Taleb and Misra [10] should read

$$\begin{aligned}\ddot{F}_s=\sum_{n=1}^{\infty}&-\left[\left\{\frac{\lambda_n^4\bar{\gamma}}{R^4}+\frac{1}{2}(C_N\dot{R}+\bar{C}_N)\psi\varepsilon\right\}\delta_{ns}+2\frac{\dot{R}}{R}(a_{ns}-c_{ns})\right]\dot{F}_n\\&+\left[\left\{\frac{\lambda_n^4\bar{\gamma}\dot{R}}{R^5}+\frac{\ddot{R}}{R}-\boxed{2\frac{\dot{R}^2}{R^2}}+\frac{1}{2}\psi\varepsilon\frac{\dot{R}}{R}(C_N\dot{R}+\bar{C}_N)\right\}c_{ns}\right.\\&+\left\{\Gamma\psi\frac{\ddot{R}}{R}+\frac{1}{2}C_T\psi\varepsilon\frac{\dot{R}^2}{R}+2\frac{\dot{R}^2}{R^2}\right\}d_{ns}-\left\{\frac{\dot{R}^2}{R^2}\right\}e_{ns}\\&+\left\{-\frac{\lambda_n^4}{R^4}+\boxed{4\bar{\gamma}\frac{\dot{R}}{R^5}\lambda_n^4}\right\}\delta_{ns}-\left\{+\frac{1}{2}(C_N\dot{R}+\bar{C}_N)\psi\varepsilon\frac{\dot{R}}{R}-\boxed{2\frac{\dot{R}^2}{R^2}}+\psi\frac{\ddot{R}}{R}\right\}a_{ns}\\&\left.-\left\{\frac{1}{2}\left[C_TR\varepsilon\boxed{+}\tilde{C}_T\right]\psi\frac{\dot{R}^2}{R^2}+\frac{\dot{R}^2}{R^2}+\Gamma\psi\frac{\ddot{R}}{R}\right\}b_{ns}\right]F_n\quad(s=1,2,\ldots\infty),\end{aligned}\tag{33}$$

where the discrepancies between Eq. (33) and Taleb and Misra's [10] are again boxed.

Appendix B. Solving for numerical values of the constants of Eqs. (28)

Constants a_{ns}, b_{ns}, d_{ns} are found analytically with expressions derived by Païdoussis [15, Table 3.1, pp. 87–88; 466–467]; note that the symbols used here are different. In the same fashion, another analytical expression is derived for c_{ns}, required here but not in Païdoussis' work. Expressions for these constants are given in Table 4. Values for e_{ns} are found by numerical integration using the composite midpoint rule.

References

[1] M.P. Païdoussis, *Fluid–Structure Interactions: Slender Structures and Axial Flow*, Vol. 2, Elsevier Academic Press, London, 2003.
[2] B.O. Al-Bedoor, Y.A. Khulief, An approximate analytical solution of beam vibrations during axial motion, *Journal of Sound and Vibration* 192 (1996) 159–171.

[3] D. Mote Jr., Dynamic stability of axially moving materials, *The Shock and Vibration Digest* 14 (4) (1972) 2–11.
[4] A. Wickert, C.D. Mote Jr., Current research on vibration and stability of axially-moving materials, *The Shock and Vibration Digest* 20 (1989) 3–13.
[5] R. Barakat, Transverse vibrations of a moving thin rod, *Journal of the Acoustical Society of America* 43 (1968) 533–539.
[6] S. Kalayacioglu, A.K. Misra, Approximate solution for vibrations of deploying appendages, *AIAA Journal of Guidance, Control, and Dynamics* 14 (1991) 287–293.
[7] B. Tabarrok, K. Behdinan, Dynamics of spacecraft antenna during deployment, in: S. Pellegrino, S.D. Guest (Eds.), *Proceedings of the IUTAM/IASS Symposium on Deployable Structures: Theory and Applications*, Kluwer, Dordrecht, 2000, pp. 415–424.
[8] M. Stylianou, B. Tabarrok, Finite element analysis of an axially moving beam, part I: time integration, *Journal of Sound and Vibration* 178 (1994) 433–453.
[9] M. Stylianou, B. Tabarrok, Finite element analysis of an axially moving beam, part II: stability analysis, *Journal of Sound and Vibration* 178 (1994) 455–481.
[10] I.A. Taleb, A.K. Misra, Dynamics of an axially moving beam submerged in a fluid, *AIAA Journal of Hydronautics* 15 (1981) 62–66.
[11] G.I. Taylor, Analysis of swimming of long and narrow animals, *Proceedings of the Royal Society (London) A* 211 (1952) 225–239.
[12] M.P. Païdoussis, Dynamics of flexible slender cylinders in axial flow. Part 1 theory, *Journal of Fluid Mechanics* 26 (1966) 717–736.
[13] R.E.D. Bishop, D.C. Johnson, *The Mechanics of Vibration*, Cambridge University Press, Cambridge, 1979.
[14] F. Gosselin, Stability of Deploying Extruding Beam in Dense Fluid, B. Eng. Honours Thesis, McGill University, Montreal, 2004.
[15] M.P. Païdoussis, *Fluid–Structure Interactions: Slender Structures and Axial Flow*, Vol. 1, Elsevier Academic Press, London, 1998.